

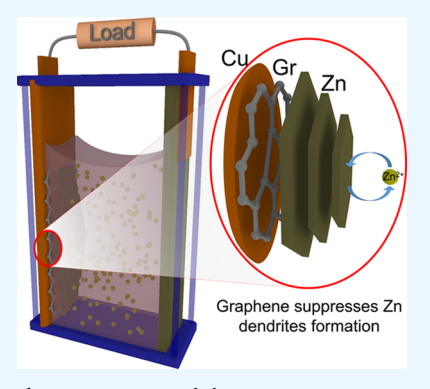
Non-Dendritic Zn Electrodeposition Enabled by Zincophilic **Graphene Substrates**

Tara Foroozan, Vitaliy Yurkiv, Soroosh Sharifi-Asl, Ramin Rojaee, Farzad Mashayek, and Reza Shahbazian-Yassar*

Mechanical and Industrial Engineering Department, University of Illinois at Chicago, Chicago, Illinois 60607, United States

Supporting Information

ABSTRACT: Rechargeable zinc (Zn) batteries suffer from poor cycling performance that can be attributed to dendrite growth and surface-originated side reactions. Herein, we report that cycling performance of Zn metal anode can be improved significantly by utilizing monolayer graphene (Gr) as the electrodeposition substrate. Utilizing microscopy and X-ray diffraction techniques, we demonstrate that electrodeposited Zn on Gr substrate has a compact, uniform, and nondendritic character. The Gr layer, due to its high lattice compatibility with Zn, provides low nucleation overpotential sites for Zn electrodeposition. Atomistic calculations indicate that Gr has strong affinity to Zn (binding energy of 4.41 eV for Gr with four defect sites), leading to uniform distribution of Zinc adatoms all over the Gr surface. This synergistic compatibility between Gr and Zn promotes subsequent homogeneous and planar Zn deposits with low interfacial energy (0.212 J/m²) conformal with the current collector surface.



KEYWORDS: zinc battery, zn dendrites, graphene electrodeposition substrate, uniform Zn deposition, zincophilic, ab initio calculations

INTRODUCTION

Zinc metal is an ideal anode material for battery systems due to its stability, environmental benignity, low equilibrium potential, multielectron redox capacity, high abundance, low cost, and safety. After the invention of Zn-MnO₂ battery systems in 1866, various primary and secondary Zn-based systems such as Zn/NH₄Cl/MnO₂, Zn/ZnCl₂/MnO₂, Zn/ KOH/MnO₂, and Zn/ZnSO₄/ MnO₂ were developed.² However, currently commercialized Zn batteries using alkaline electrolytes are either nonrechargeable or poorly rechargeable due to pronounced precipitation of zinc oxide (ZnO) that can reversibly passivate the electrode surface and cause battery failures.³ Recently, mild electrolyte systems are governing the new battery systems such as Zn-MnO₂, Zn-V₂O₅, Co₃O₄-Zn, and Ni-Zn mainly after achieving 5000 cycles with adapting the new conversion mechanism and breaking the 2 V barrier in Zn aqueous batteries.⁴⁻⁷ Considering the great contribution of mild aqueous batteries offering environment friendliness, long cycling stability, and high voltage, the main remaining challenge is the dendritic and nonuniform deposition of Zn, which is the focus of this paper. Zn²⁺ ions prefer to deposit on local inhomogeneities with high localized current density existing on the substrate surface, which leads to the formation of ramified Zn dendrites with high surface area. The Zn dendrites with very high Young's modulus (~100 GPa) can easily penetrate the cell separator and reach the counter electrode causing an internal short circuit and release of uncontrolled heat and energy, which is a safety concern.8 In addition, dead Zn formation and surface-originated side reactions (e.g., corrosion and H2 evolution) and oxide passivation amplified by high-surface-area zinc dendrites may lead to capacity loss and short cycle life in Zn-based batteries.^{3,9}

Various strategies have been employed to suppress the dendritic electrodeposition of Zn. Engineering the electrolyte composition by inorganic (metal salts, oxides, and hydroxides) and organic (polymers or surfactants) additives has shown some effect on alleviating zinc electrode corrosion and suppression of Zn dendrites. 10,11 Structural design approaches such as three-dimensional (3D) Zn sponge, 12 anion-exchange ionomer-coated Zn sponge, 13 conductive Zn/Cu foam, 5,14 3D graphite fibers, 15 and cross-linked polyacrylonitrile (PAN)based cation-exchange membrane 16 are among other approaches used for suppression of Zn dendrites. The main goal in these approaches is to increase the surface area of Zn to enhance the distribution of the Zn ions and reduce the side reactions associated with Zn shape changes. 10,11,17 Additionally, protective coating of the Zn particles with bismuth-based oxides (such as Bi₂O₃, Bi₂O₃-Li₂O-ZnO, and Bi₂O₃-ZnO-CaO)^{18,19} and reduced graphene oxide (rGO)²⁰ have been used to reduce Zn degradation by capturing the zincate ions (Zn(OH)₄²⁻) inside the anode and providing a conductive network between Zn particles. Mechanical suppression of Zn dendrites has been also achieved by utilizing rGO²¹ and

Received: July 25, 2019 Accepted: November 1, 2019 Published: November 1, 2019



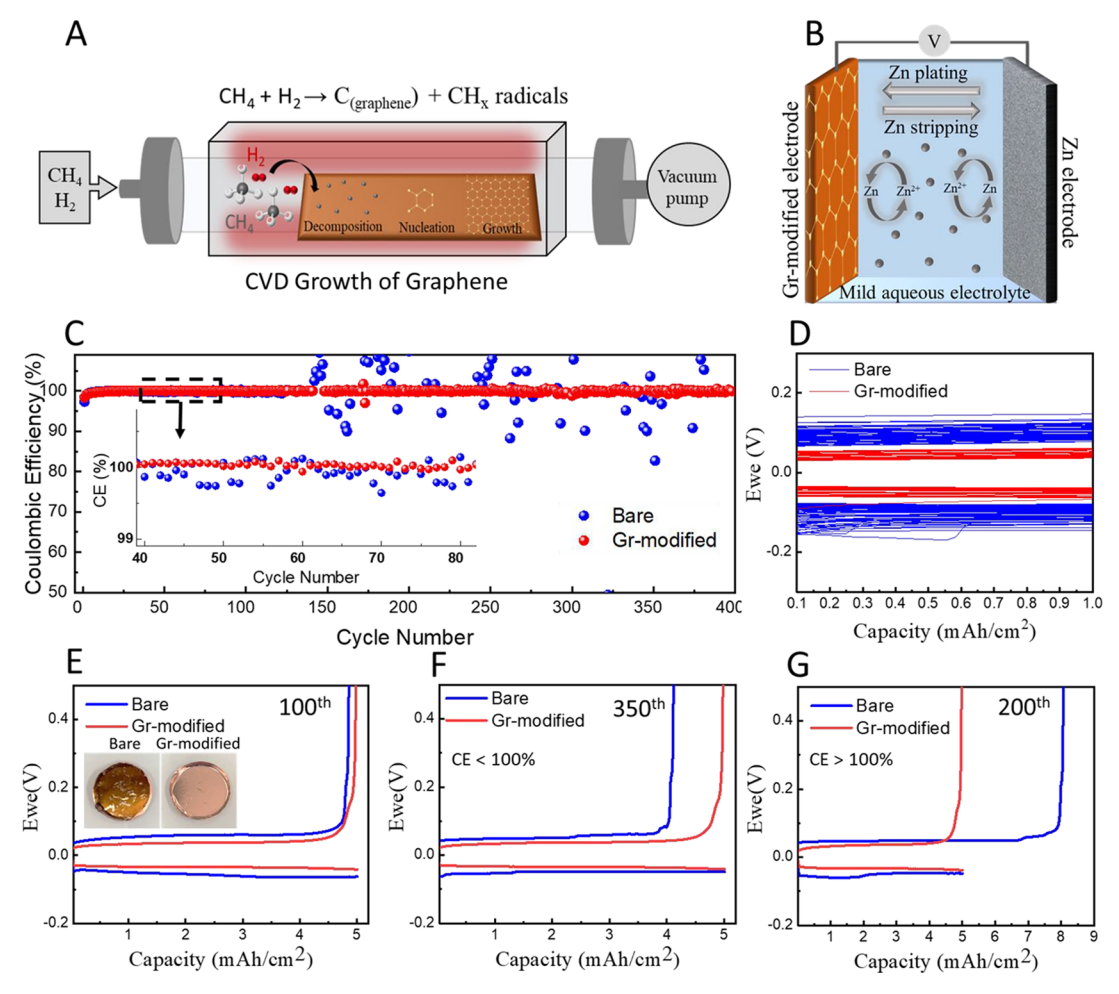


Figure 1. Schematic diagram of CVD growth of Gr and the cycling performance of Zn metal anode on the bare and Gr-modified electrodes. (A) CVD growth of Gr on Cu foil. (B) Raman spectra obtained from CVD-grown monolayer Gr. (C) Coulombic efficiency test for the bare and Grmodified electrodes at 5 mA/cm² current density and 5 mAh/cm² capacity. Inset shows the magnified CE% profile for cycles 40-80. (D) Voltage hysteresis profile. Charge/discharge curves observed for the bare and Gr-modified electrodes for (D) 100th, (E) 350th, and (G) 200th cycles. The insets in (E-G) show optical images obtained from the bare and Gr-modified electrodes showing similar behaviors as the cycling profiles shown in (E-G).

TiO₂²² coatings and Zn back-plating approach.⁸ However, the difficulty in controlling the additives' stability and amount over prolonged cycling, inactive mass additions, nonhomogeneous physical mixtures, and loose contact between coating and Zn particles lead to increased cell resistance and complicate the battery performance.

Furthermore, the choice for current collectors in aqueous Zn-based batteries is limited due to the interplay between several requirements such as electrical conductivity, environmental stability, low weight, and cost. Copper fits all of these criterions; however, the use of Cu in aqueous Zn batteries is challenging due to metal dissolution and corrosion.²³ For this purpose, more noble materials such as stainless steel and titanium, which are less susceptible to corrosive attack, are primarily used as current collectors for Zn.24 However, the high cost and lower electrical conductivity of these materials are the drawbacks of utilizing such current collectors. Meanwhile, it has been shown that substrate can directly affect zinc deposition morphology by altering the overvoltage of parasitic hydrogen evolution reaction (HER), zinc deposition kinetics, or crystallographic growth habit of Zn. 11,25

Herein, we propose utilizing a monolayer graphene directly grown on the Cu current collector surface to be used as the Zn

electrodeposition substrate. The idea is to utilize an ultrathin conductive coating on the Cu current collector that can simultaneously suppress the dendritic deposition of Zn and also passivate the Cu surface against side reactions in aqueous electrolytes. It has been shown that Gr does not allow for permeation of various molecules such as O2 and H2O in the out-of-plane direction;²⁶ hence, it is as an effective protective coating against corrosion.^{27,28} Therefore, Gr-coated Cu can be potentially an applicable current collector in aqueous batteries. In addition, Zn and Gr both have hexagonal lattice structures with small lattice mismatch (~8%),²⁹ which is an important parameter in designing and construction of suitable electro-deposition matrices. ^{30,31} The modification of Cu substrate with Gr leads to a significant alteration in the morphology of Zn electrodeposits, achieving a compact and uniform structure that results in highly improved electrochemical stability of Zn metal anode. Density functional theory (DFT) modeling results revealed that graphene has high affinity to Zn metal, making it a highly zincophilic substrate with low interfacial energy that alters the nucleation and growth mechanism of Zn. Combining the fundamental understandings coming from this work and the high-throughput methods for Gr production such as roll-to-roll CVD32 and liquid-phase exfoliation,33 we see a great potential for utilization of Gr as a substrate for long-life and stable Zn metal batteries.

■ RESULTS AND DISCUSSIONS

Gr-modified electrodes were fabricated by direct growth of graphene on copper foil using the chemical vapor deposition (CVD) method (see Methods), as schematically depicted in Figure 1A. During the growth procedure, the Gr grains gradually grow and connect with each other and coalesce into a continuous monolayer graphene layer. Optical and SEM images in Figures S1 and S2 show how partially covered Gr develops into full coverage Gr by increasing the growth time. Raman spectroscopy is a powerful tool for characterizing graphene showing three prominent peaks of the so-called G band appearing at 1582 cm⁻¹, the 2D band at about 2700 cm⁻¹, and the disorder-induced D-band at around 1350 cm⁻¹ using a laser excitation of 532 nm. The significantly lower G peak intensity compared to 2D peak in Figure S3 obtained from our CVD-grown Gr confirms its monolayer nature.3 Both optical images and Raman spectra were obtained from Gr films transferred to the Si/SiO2 substrate due to better optical color contrast, intensified Raman scattering, and lower spectral background obtained on Si/SiO₂ compared to Cu.³⁵ The asprepared Gr-coated Cu foil (called Gr-modified electrodes throughout the paper) were directly utilized as electrodes. The schematic in Figure 1B shows the half-cell configuration used for studying the electrochemical and morphological behavior of Zn on Gr-modified electrodes.

To evaluate the cycling stability, half-cell batteries containing Zn foil as a counter electrode and bare/Gr-modified Cu as a working electrode were assembled for galvanostatic cycling tests. Mild aqueous ZnSO₄ solution (pH ~4) was used as an electrolyte. Zn electrodeposition was carried out at a current density of 5 mA/cm² for 1 h on the bare/Gr-modified Cu electrode. Then, the current was reversed to strip and redeposit the Zn back onto the counterelectrode. Cutoff voltage for the stripping process is configured to be 1.0 V. Herein, the Coulombic efficiency (CE) was calculated based on the ratio of Zn stripping and plating capacity in each cycle. As shown in Figure 1C, the bare Cu electrode shows stable cycling performance for less than 150 cycles. The decreased CE and unstable cycling of Zn ions after prolonged cycling could be due to the large surface area of Zn dendrites that promotes the surface-originated, detrimental side reactions. In contrast, stripping/plating of Zn on the Gr-modified electrode was highly stable and reliable for more than 400 cycles under identical electrochemical conditions. The inset in Figure 1C shows the CE% performance for cycles 40-80. Although the cycling stabilities of the bare and Gr-modified electrodes are in close range for the first 100 cycles, small fluctuations can be detected in the bare sample. Additionally, as shown in Figure 1D, Zn deposition on graphene substrate requires a lower cycling overpotential (0.02-0.03 V) compared to that on the bare electrode (0.04-0.1 V), which remains more stable throughout the cycling experiment. This observation signifies a more facile deposition/stripping process occurring in the presence of Gr. Figure 1E shows the voltage profile for the 100th cycle of charge/discharge, where CE is ~100% for the Gr-modified electrode and ~99.5% for the bare sample. To identify the source of this small capacity decay of the bare electrode, a typical cell was opened after the complete dissolution of Zn. Interestingly, a brownish surface was detected in the case of the bare electrode, in contrast to the

fresh and shiny surface of the Gr-modified electrode (cf., inset of Figure 1E). Figure S4 compares the high-magnification optical image of the brownish film formed on the surface of the bare Cu with the almost intact surface of the Gr-modified electrode. The different colors observed in the optical image show that the film is composed of different compounds. Dark red and black colors detected can be correlated to copper(I) and copper(II) oxides, respectively.³⁶ X-ray photoelectron spectroscopy (XPS) also confirms that the brownish film is composed of oxides of both Cu and Zn. The details can be found in Figure S5. After surpassing ~140 cycles, anomalous cycling behavior is observed in the bare sample, where the discharge capacity is either smaller or larger than the charge capacity (Figure 1F,G). The decreased discharge capacity (e.g., cycle Figure 1F), which indicates smaller fraction of available Zn for stripping, can be correlated to dead (electrochemically inactive) Zn formation and Zn passivation that occur as a result of dendritic zinc deposition and zinc oxide (ZnO) layer formation. During cycling and shape change of Zn, if the dead Zn re-establishes an electrical connection to the underlying Zn, then a Coulombic efficiency of higher than 100% can be observed.37,38 In addition, detrimental dissolution and oxidation of the Cu current collector in aqueous environment can be partially responsible for the excess capacity.

Immersion, electrochemical impedance spectroscopy (EIS), and Tafel polarization tests were utilized to justify the effectiveness of Gr in impeding the corrosion of the Cu electrode surface. Immersion test was performed by soaking bare and Gr-modified Cu electrodes in the electrolyte for 30 days before studying the morphological changes as a result of corrosion and dissolution. Figure S6A shows the highly porous and nonuniform surface of bare Cu after significant dissolution happening in contact with the ZnSO₄ electrolyte. However, only minor degradation is observed on the surface of the Grmodified electrode (Figure S6B), which can be a result of inherent defect sites existing on Gr and electrolyte permeation under the graphene surface. ²⁸ The result of our EIS measurement on bare and Gr-modified Cu electrodes and the corresponding schematic of the electrical equivalent circuits (EEC) are shown in Figure S7. Table S1 shows R_1 (electrolyte resistance), R_2 (surface coating), and R_3 (metal/ electrolyte interface) resistances. The mathematical sum of R_2 and R_3 (Table S1) is a measure of the corrosion resistance, which is significantly higher in the case of the Gr-modified electrode. In addition, the Tafel fitting of the potentiodynamic polarization data in Figure S8 exhibits a higher corrosion current density (i_{corr}) and lower corrosion potential (E_{corr}) for the bare Cu. Meanwhile, Gr coating decreased the passivation current density (i_{pass}) of copper to 124 μ A cm⁻², which shows about 50% reduction compared to the pristine copper electrode. It is worth noting that the open circuit potential (E_{OCV}) of the copper electrode shows a slight increase after modifying the surface with graphene monolayer, which can be attributed to physicochemical changes of the surface. This observation is consistent with those previously reported in the literature. 27,28 Table S2 summarizes these results. Abovementioned results suggest the increase in the resistance of the metal to electrochemical degradation and corrosion by using the Gr passivating layer on copper. Although the discussed results demonstrate the increased resistance of the current collector to electrochemical corrosion by using the Gr passivating layer on copper, galvanic corrosion of the Zn metal being at the low end of galvanic series would remain as

an active corrosion mechanism with almost any metallic current collectors. 40 We should note that Gr has been widely used as an anticorrosion coating in both acidic and basic environments; ^{39,41,42} therefore, its effectiveness in improving the Zn electrodeposition morphology can also be investigated in the Z-alkaline battery systems.

To reveal the underlying mechanism of improved electrochemical cycling, the electrodeposited Zn on the graphene and bare Cu substrates was fully characterized. Zn (5 mAh/cm²) was deposited on bare and Gr-modified Cu substrates using the same electrolyte and current density that were utilized in the cycling experiments. Electrodeposition products on the surface of bare Cu appeared with a grayish color, which developed into a black color by further deposition (bottom right inset of Figure 2A). The gray deposition is an indication of the coarse boulder-like Zn deposition composed of stacks of irregular platelets. Upon further Zn plating, the boulder-like structures develop into blackish large-surface-area Zn dendrites, 43 as confirmed in the high-magnification SEM images shown in Figure 2A. The stepwise development of Zn dendrites on top of local surface protuberances with high

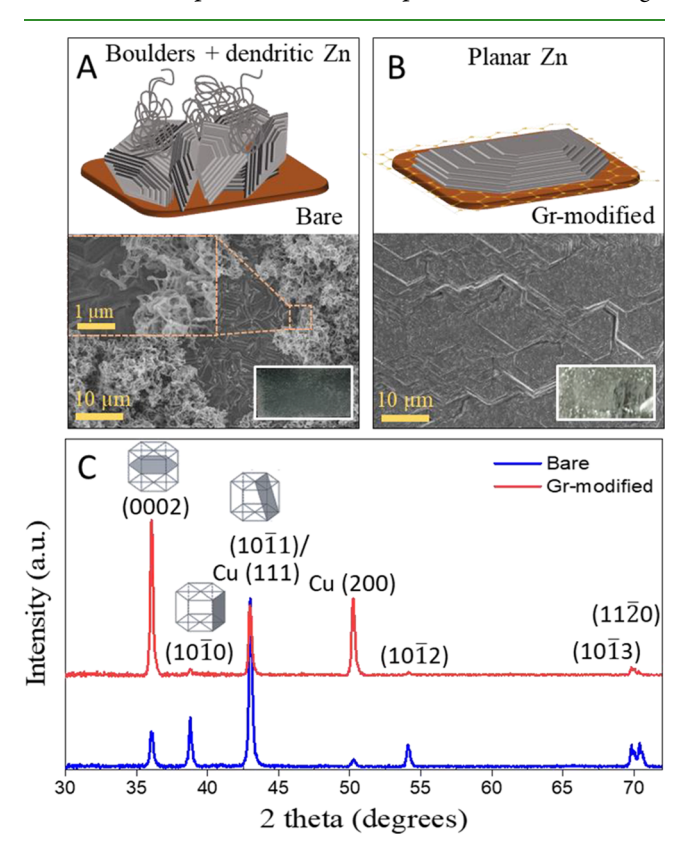


Figure 2. Zn electrodeposition morphology and crystal growth preference in the case of the bare and Gr-modified Cu electrodes. (A) Dendritic and nonuniform Zn dendrites grown on top of randomly oriented Zn boulders are observed in the case of bare Cu. Top-left inset shows the initiation of Zn dendrites on top of Zn boulders. Bottom-right inset is the optical image of dark-colored Zn dendrites deposited on the bare substrate. (B) Highly planar and nondendritic Zn hexagons observed in the case of the Gr-modified substrate. Inset is the optical image of the substrate showing shinny and crystalline Zn deposition. (C) GIXRD pattern shows the highly oriented growth direction of Zn parallel to the Gr-modified Cu electrode surface, in contrast to the randomly oriented Zn deposition in the case of the bare sample.

local current density existing on Zn boulders is shown in Figure S9. The current density of 10 mA/cm² was used in all the samples with different Zn deposition capacities of 3, 6, and 10 mAh/cm² for Figure S9A-C, respectively. Optical images in the insets show the change in color of Zn deposits from bright to dark gray by evolution of Zn dendrites. The observed morphology is an indication of field-oriented crystals (containing dendrites and loose crystals) expected at such high current density deposition, where continuous 2D nucleation on filaments is promoted.⁴⁴ The SEM image in Figure \$10 shows the initiation of Zn filament on top of the Zn boulder's edge sites. Interestingly, depositing Zn on the surface of the Gr-modified electrode resulted in shiny and metallic Zn deposition (inset of Figure 2B). The highly bright finish and reflective color of the deposit confirm the formation of compact and nonporous metallic Zn on the Gr-modified substrate. 45 SEM imaging showed highly planar Zn hexagon crystals parallel to the electrode surface in the case of the Grmodified electrode (Figure 2B). Figure S11 shows the lowmagnification image of the bare and Gr-modified substrates for uniformity comparison.

Grazing incidence X-ray diffraction (GIXRD) was performed to compare the crystalline structure of Zn deposition products on the surface of bare and Gr-modified Cu substrates. As can be seen in Figure 2C, (0002), $(10\overline{1}0)$, $(10\overline{1}1)$, $(10\overline{1}2)$, $(10\overline{13})$, and $(11\overline{20})$ planes are detected for Zn electrodeposited on the bare Cu surface, showing the random orientation of both boulders and dendrites. Previous works summarized the affiliation between zinc morphology and its alignments to the substrate. 46–48 Accordingly, the basal-type growth of Zn (exhibiting $0-30^{\circ}$ alignment to the substrate) possesses preferred crystallographic planes of (0002) and $(10\overline{1}3)$. $(10\overline{1}2)$ and $(10\overline{1}1)$ are intermediate (triangular) planes, which favor 30-70° alignment of Zn growth to the substrate, whereas $(10\overline{1}0)$ and $(11\overline{2}0)$ support Zn growth with alignment of 70-90°. Based on this understanding, the predominant (1010) and (1120) planes of Zn electrodeposition are affiliated with Zn dendrites grown on bare Cu substrate. However, the Zn deposition on the Gr substrate has a different growth preference as the dominant crystalline orientation of Zn deposition products is switched to (0002), which supports the basal growth of Zn parallel to the Cu surface and (100), $(10\overline{12})$, and $(11\overline{20})$ planes almost vanished. The dominant crystal planes of hexagonal close-packed (hcp) Zn are also depicted for clarity. We should note that the intense (1011) facet of Zn overlaps with the (111) Cu surface existing in our Cu foil. The dominance of (0002) facets and the absence of $(10\overline{10})$ and $(11\overline{20})$ planes correspond to uniform and nondendritic Zn electrodeposition, which mitigates the H₂ evolution, corrosion, dead Zn formation, and Zn dissolution. To evaluate the effectivity of the graphene substrate in improving the Zn deposition morphology over long cycling, grazing incident XRD (GIXRD) measurements were carried out on the bare and Gr-modified electrodes after 30 cycles (at a current density of 5 mA/cm² for 1 h at the charged, fully deposited state). As can be seen in Figure S12, nonuniform and randomly oriented Zn flakes are detected on the bare sample, while highly compact layers of horizontally sitting Zn are observed on the Gr-modified electrode. Comparing the intensities of GIXRD peaks at $\sim 36^{\circ}$ ((0002) plane parallel to the electrode surface) and $\sim 39^{\circ}$ ((1010) plane vertical to the electrode surface) shown in Figure S13 can be considered as an indicator of Zn deposition

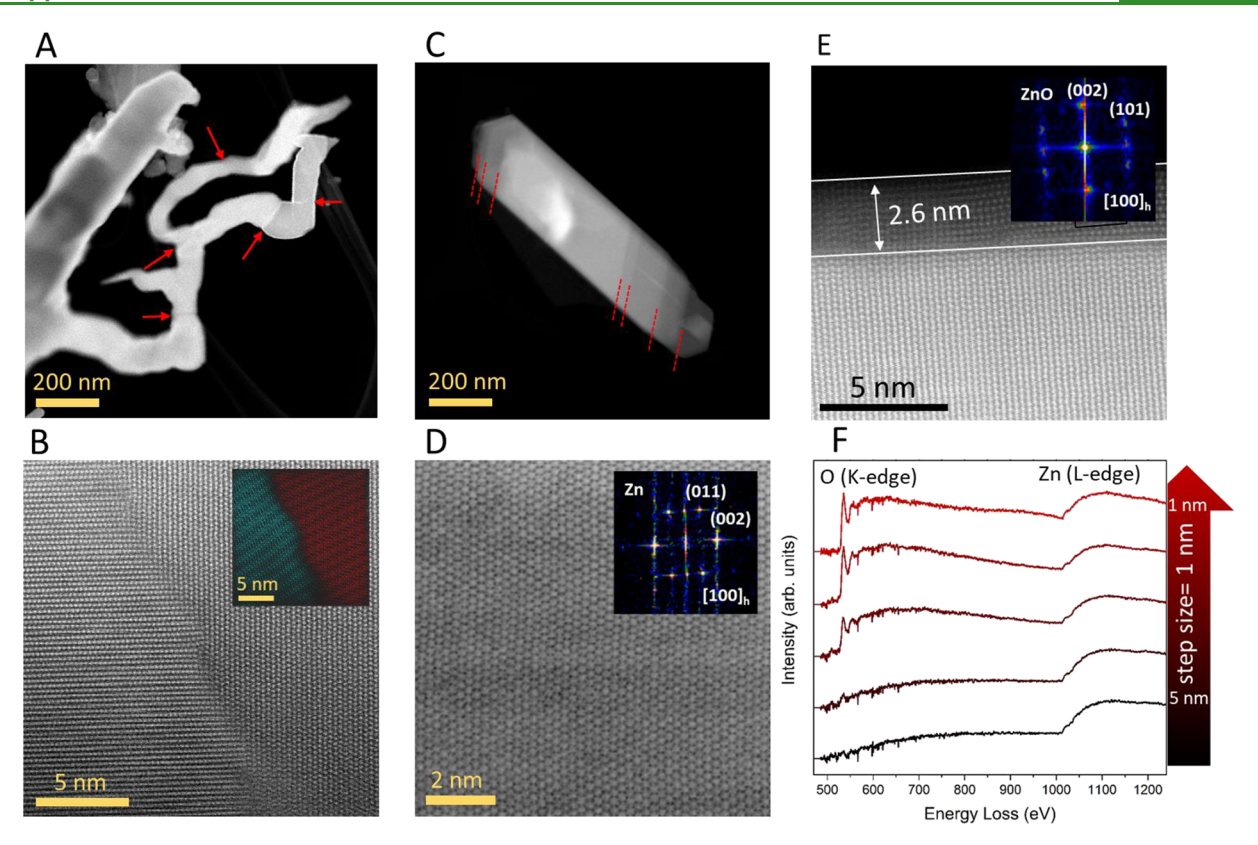


Figure 3. Annular dark-field imaging from Zn deposits on bare and Gr-modified Cu. (A) Low-magnification LAADF image shows a branch of Zn dendrites with polycrystalline nature. The red arrows show some of the grain boundaries at which the orientation of Zn growth changes. (B) Atomic-resolution image obtained from Zn dendrites near the grain boundary. Inset shows the color-coded image that better demonstrates the change in the Zn dendrite growth orientation. (C) Low-magnification annular dark-field image shows planar Zn hexagons grown on the Grmodified electrode. The red dash lines show the parallel planes of Zn grown on top of each other. (D) Atomic-resolution image obtained from planar Zn grown on the Gr-modified electrode. Inset shows the corresponding FFT pattern that is indexed as the [100] zone axis of the hexagonal Zn structure. (E) Atomic-resolution STEM image from the surface of Zn deposits showing a ~2.5 nm oxide layer at the surface. Inset shows the corresponding FFT pattern that is indexed as the [100] zone axis of the hexagonal ZnO structure. (F) EELS spectra confirming the thickness of the oxide layer to be ~ 2.5 nm with a 1 nm step size.

morphology. Accordingly, a considerable increase in the $(0002)/(10\overline{10})$ peak ratio in the bare sample from 0.35 to 1.7 in the Gr-modified sample corresponds well to the more planar Zn morphology on the Gr-modified Cu electrode, which is maintained even after long cycling.

The electrodeposition behavior of Zn on bare and Grmodified Cu was also evaluated at current densities higher and lower than 5 mA/cm². SEM images obtained from 5 mAh/cm² Zn deposited on bare and Gr-modified Cu at current densities of 10 and 15 mA/cm² are shown in Figure S14. At a current density of 10 mA/cm², the expected randomly oriented boulders were detected on the bare electrode and no mossy dendrites formed (Figure S14A). It is known for Zn metals that mossy dendrites more easily formed at lower current densities. 44,49 Interestingly, the layered Zn deposition is maintained on Gr-modified electrodes (Figure S14B). By increasing the current density even more to 15 mA/cm², vertically aligned Zn is observed on the bare Cu electrode (Figure S14C), while lateral growth of Zn on the Gr-modified electrode is maintained to a good extent (Figure S14D). By lowering the current to 2 mA/cm² (Figure S15), a different behavior is observed. Overall, at low current densities, the nonuniform Zn can easily evolve even on top of highly planar Zn, which is due to the effect of local current disturbance happening at surface protuberances.⁴⁴ In the case of the bare electrode, even after a short deposition time (capacity of 2

mAh/cm²), mossy Zn deposition is observed (Figure S15A). This behavior is lessened on the Gr-modified electrode having highly planar Zn hexagons formed with locally evolved bulges composed of randomly oriented Zn flakes (Figure S15B). Overall, the uniformity of Zn deposition improved on Grmodified electrodes in all the current densities used. To realize the full potential of this proposed system, long-term stability of electrodeposited Zn anodes on Gr@Cu substrates should be investigated in Zn-based energy storage systems such as Zn// carbon hybrid capacitors⁵⁰ and Zn/MnO₂⁵ batteries.

Aberration-corrected scanning transmission electron microscopy (AC-STEM) was utilized to obtain Z-contrast high-angle annular bright-field (HAADF) and defect sensitive low-angle annular bright-field (LAADF) images, which provide insights into the atomic structure of the samples. Additionally, chemical composition and valence state analysis were carried out by means of electron dispersive spectroscopy (EDS) and electron energy loss spectroscopy (EELS). Figure 3A demonstrates an LAADF image from a Zn dendrite grown on bare Cu substrate. The branch-like dendrite does not have a defined shape with sharp tips capable of penetrating the separator and causing a short circuit. Figure S16 shows an example of Zn dendrites puncture and their penetration through the separator. Also, it can be seen that Zn dendrites change their growth direction and form kinks, favoring ramified growth of more dendrites. Formation of such kinks was also observed during the growth

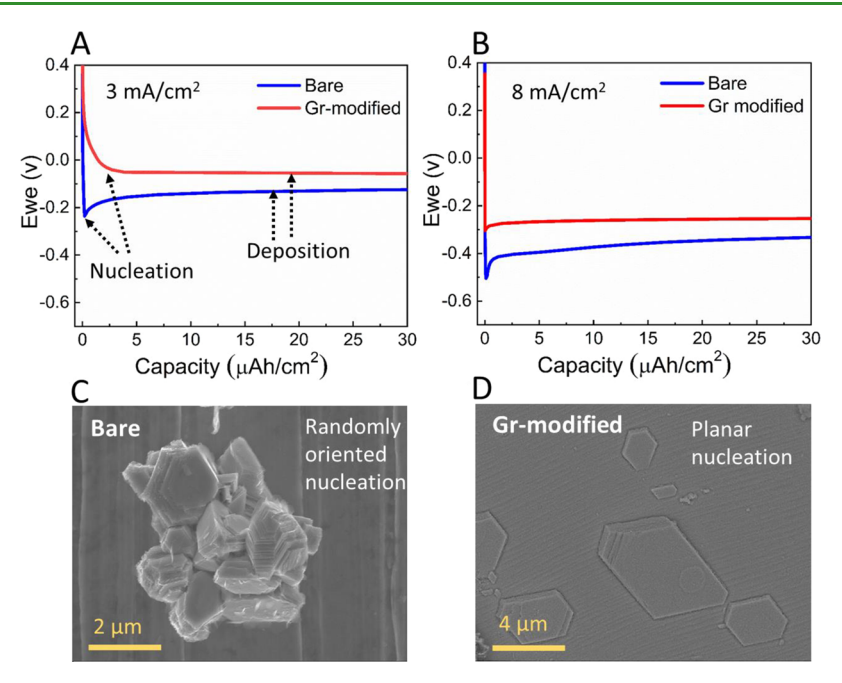


Figure 4. Zn nucleation behavior on bare and Gr-modified Cu electrodes. (A) Voltage—time curve during nucleation in the case of bare and Gr-modified Cu at a current density of 3 mA/cm². (B) Voltage—time curve during nucleation in the case of bare and Gr-modified Cu at a current density of 8 mA/cm². (C) Zn nuclei composed of randomly oriented Zn platelets formed on the surface of bare Cu. (D) Zn nuclei composed of highly planar platelets parallel to the electrode surface are formed in the case of the Gr-modified electrode.

of Li filaments.31 However, it is recently shown that kink formation in Li dendrites does not induce any crystalline heterogeneity, and the change in the direction of growth can be attributed to the variation of the SEI composition and/or structure during the growth of Li dendrites.⁵¹ In contrast, the change in the growth direction of Zn dendrites is accompanied by grain boundary formation and formation of a new Zn grain, as confirmed by the lines in the LAADF image that corresponds to a discontinuity in the crystal structure and formation of polycrystalline dendrites. An atomic-resolution HAADF image from a kink in a Zn filament that corresponds to a grain boundary is shown in Figure 3B. A color-coded image (shown in inset) is reconstructed based on the distinct fast Fourier transform (FFT) patterns from each phase. Both grains correspond to the [010] zone axis of the pure Zn with a hexagonal crystal structure from the P63/mmc space group, which are angled with respect to each other. This denotes an abrupt change in the growth direction during the deposition. We should note that the grain boundaries are not favorable in Zn deposits as the atoms at the grain boundaries have higher reactivity, introducing more active sites for H₂ gas evolution and corrosion.⁵² In addition, the existence of defects and grain boundaries provokes surface protuberances, which can lead to overgrowth of Zn dendrites.⁵³ On the other hand, extracted particles from the Gr-modified substrate have a highly defined morphology, which denotes a more uniform and controlled Zn deposition process. An example is shown in Figure 3C, which is a plate-like Zn deposit. This large micron-size Zn deposit is a single crystalline structure as no grain boundary could be detected in any region when inspected by atomic resolution imaging. Additionally, it can be observed that the growth of this particle continued by formation of new layers over previous layers, which allows for a layered, uniform Zn deposition in the [100] direction, as revealed by the atomicresolution HAADF image shown in Figure 3D. This type of crystal growth is the preferred growth direction for Zn metal

anodes that upon accumulation forms compact, layer-like, and reflective Zn configuration, which is hardly achievable in nonmodified samples. 54,55

Noteworthy, an ultrathin layer (2-3 nm) of oxide is detected on the surface of Zn deposits in both samples, as shown in Figure S17. Atomic-resolution imaging and corresponding FFT analysis in Figure 3E confirm the oxygen-containing layer to be hexagonal ZnO crystals from the P63mc space group. Figure S18 shows the unit cell models for hexagonal P63/mmc Zn and hexagonal P63mc ZnO. It should be noted that the identified thickness of ZnO formed in the mild 2 M ZnSO₄ electrolyte is much smaller than the oxide film formed on the Zn surface in the case of alkaline electrolytes (>2 μ m). ^{56,57} The EELS map analysis (Figure 3F) was also employed to confirm the thickness and chemical composition of the ZnO layer. Since the ZnO formation is known to be a surface-originated phenomenon, it stresses the significance of reducing the surface area through alteration of deposition morphology in improving the electrochemical properties of Zn batteries. To understand how the deposition morphology and time affect the overall composition of the electrodeposited material, we performed X-ray photoelectron spectroscopy (XPS) depth profile analysis. Samples were composed of 8 mAh/cm² electrodeposited Zn (~1.1 mmthick) on the bare and Gr-modified Cu substrates with a current density of 10 mA/cm². Figure S19 shows the XPS survey spectra obtained from both bare and Gr-modified electrodes, indicating zinc and oxygen as the main components. Figure S20A,B shows the atomic concentration profiles of Zn and O for bare and Gr-modified samples, which can be correlated to the composition of gradually deposited Zn at different stages of electrodeposition. Evidently, the Zn/O ratio is higher in the Gr-modified sample throughout the measured depth profile. The smaller amount of oxygencontaining compounds in the case of Gr-modified samples can be attributed to the deposition of compact and uniform Zn

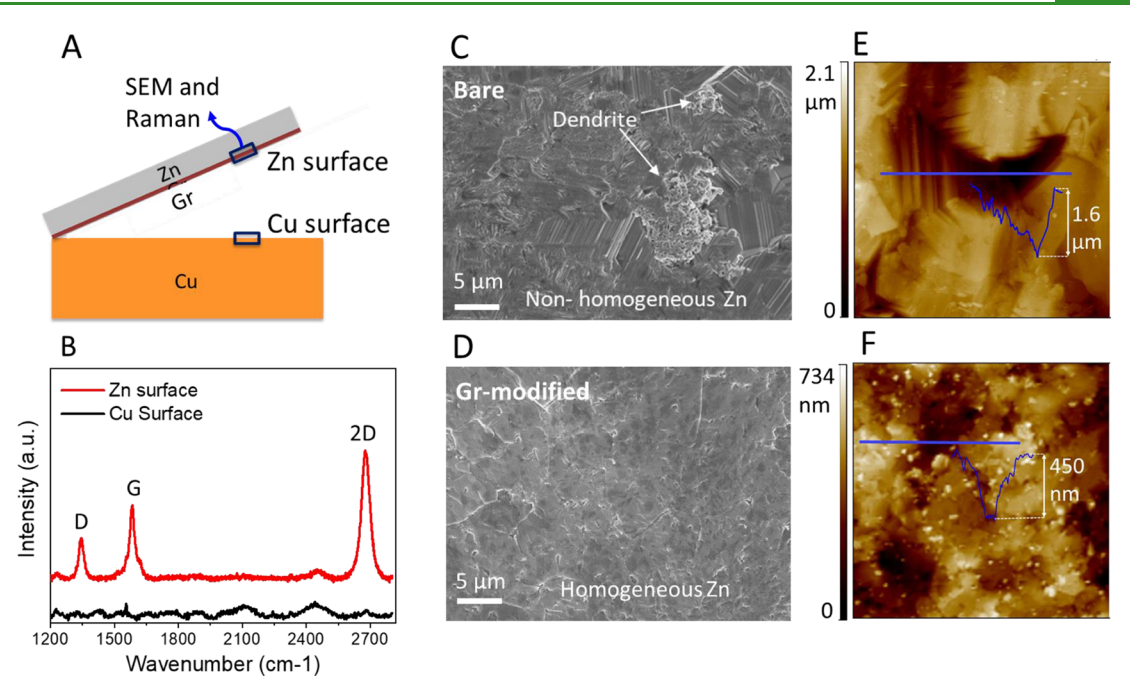


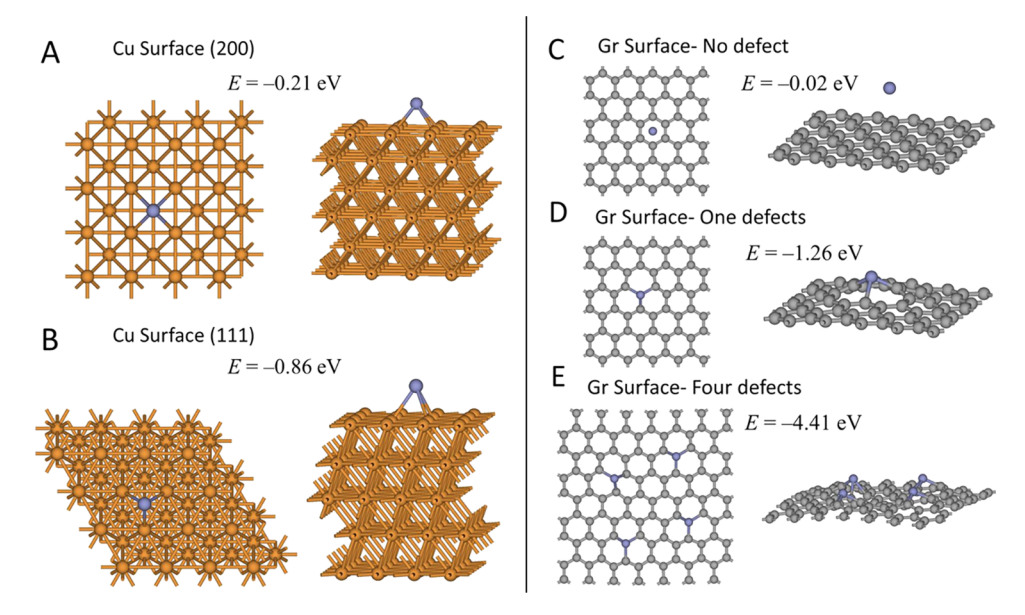
Figure 5. Zn electrodeposition behavior at the Zn/current collector interface. (A) Schematic showing the mechanical delamination of electrodeposited Zn from the Gr-modified Cu current collector surface to identify if Zn deposits directly on the Gr surface. (B) Raman spectra obtained from the Zn and Cu surfaces shown in schematic (A) after mechanical delamination, showing the existence of Gr on the surface of Zn and not Cu. SEM images obtained from the back surface of Zn delaminated from (C) bare and (D) Gr-modified Cu electrodes. AFM images of the back surface of Zn delaminated from (E) bare and (F) Gr-modified Cu electrodes. The scale of both (E, F) images are 20 × 20 μm².

with less exposed surface areas and controlled surfaceoriginated side reactions. In contrast, ramified growth of high-surface-area Zn dendrites intensifies the surface-originated detrimental reactions such as H_2 evolution, corrosion, Zn dissolution, and ZnO formation.⁵⁸ It is observed that the overall amount of oxygen-containing compounds decreases in both samples by moving from the electrolyte-facing surface toward the core of the deposition. This behavior can be explained based on the Pourbaix diagram of zinc. 59 In the mild acidic environment of our system, Zn oxidation accompanying Zn corrosion and H₂ evolution is unavoidable.⁶⁰ During prolonged Zn deposition and H2 evolution, the pH of the system gradually increases, making the system neutral or slightly alkaline, in which more stable Zn corrosion products (such as ZnO and Zn(OH)₂) are generated. Figure S20C,D shows the fitting result of O 1s spectra after 100 and 700 s of sputtering, confirming the existence of ZnO and Zn(OH)2 compounds.

It is known that the nucleation morphology has a defining role in the morphology of the final electrodeposited thin film. 55,62 Accordingly, suppression and alteration of Li dendrite growth have been achieved via modification of the electrode matrix by materials with high affinity to Li (lithiophilicity), either in the form of nucleophilic matrices 63,64 or melt-infused Li composites. 65,66 Therefore, we studied the deposition behavior of Zn at the nucleation stage to understand the origins of the uniform succedent Zn deposition morphology. The overpotentials of Zn plating on the bare and Gr-modified Cu foil induced by different binding strengths can be used to evaluate the degree of zincophilicity on the electrode surface quantitatively. At the beginning of deposition, the nucleation overpotential, which exists only in the short nucleation stage and is induced by different binding strengths between Zn and the substrate, is defined as the difference between the sharp tip

voltage and the later stable voltage plateau (mass-transfercontrolled overpotential).⁶⁷ The overpotential behavior of Zn at the early stages of deposition at two different current densities of 3 and 8 mA/cm² was studied. As it can be seen in the voltage profile of Zn metal deposition (Figure 4A,B), a noticeable difference in both the nucleation (sharp voltage tip) and deposition overpotentials (voltage plateau) was observed between the bare and the Gr-modified samples. A very smooth platform with almost no peak is observed for the Gr-modified sample, which contrasts with the 100 and 170 mV nucleation overpotentials observed for the bare sample at 3 and 8 mA/ cm², respectively. The same rule is valid for the deposition overpotential, identified as the plateau detected in the voltagetime curve. The flat voltage plateau portion is much lower for the Gr-modified electrode (50 mV at 3 mA/cm² and 200 mV at 8 mA/cm²) than for the bare electrode (120 mV at 3 mA/ cm² and 350 mV at 8 mA/cm²), which confirms the more homogeneous Zn deposition on the surface of the Gr-modified electrode. Additionally, the rate of nucleation has been increased by adding the Gr layer to the Cu substrate, as shown in Figure S21 (the details can be found in the Supporting Information).

To visually compare the nucleation morphology of Zn on bare and Gr-modified electrodes, a small amount (50 µAh/ cm²) of Zn was deposited on the bare and Gr-modified Cu electrodes with a current density of 10 mA/cm². The SEM image shown in Figure 4C demonstrates that Zn nucleation on the bare Cu results in separate Zn clusters that are composed of randomly oriented planes. In longer deposition times, these nucleates aggregate together to lower their surface energy and form boulder-type Zn deposits with high edge sites, favoring the unwanted high-aspect-ratio Zn dendrites (shown in Figure 2A). 44,68 In contrast, flat and uniform Zn deposits with hexagonal shape were nucleated on the Gr-modified electrodes



-0.86 eV), (C) pristine Gr (E = -0.02 eV), (D) Gr with single defect (E = -1.26 eV), and (E) Gr with four defects (E = -4.41 eV).

(Figure 4D). Zn layers were deposited in (0001) directions forming a flat layered structure, which is an ideal deposition morphology with minimum surface-to-bulk ratio.

To determine whether Gr acts as a suitable zincophilic substrate for Zn deposition or acts as a suppressive coating for suppression of Zn dendrites (similar to the mechanism of Li deposition on Gr/Cu substrates), we directly characterized the Zn/Gr/Cu interfaces. Initially, 8 mAh/cm² of Zn with a current density of 10 mA/cm² was deposited on the Grmodified electrode. After the deposition process, the electrodeposited Zn film was mechanically delaminated from its substrate. Raman spectroscopy and SEM imaging were carried out on both Zn and Cu interfaces. Figure 5A schematically illustrates the surfaces on which the Raman spectroscopy and SEM imaging are conducted. Raman data shown in Figure 5B demonstrates the presence of a graphene layer underneath the delaminated Zn. No Gr signal was detected from the Cu substrate, which was the original substrate for the Gr layer. This observation directly demonstrates the preferred deposition of Zn on the Gr surface. Additionally, delamination of the Gr layer from its original Cu substrate denotes the zincophilicity of Gr and the strong Gr-Zn bonds formed during electrodeposition. To verify the stability of Gr coating over long cycling, Raman spectra (Figure S22) and SEM images (Figure S23) were obtained from the surface of Grmodified samples after 30 cycles at the full discharge (stripped Zn) state. As it can be seen in Figure S22, the Raman spectra clearly indicate the presence of Gr after long cycling with small amplification in the D peak signal. Lucchese et al. carefully characterized the relation between the ratio of the D to G peak intensities (I_D/I_G) and graphene defect density,⁶⁹ which was used to evaluate the quality of Gr coating before and after cycling. The I_D/I_G is 0.3 for the pristine sample, which translates to an interdefect distance of 14 nm. The small increase in the intensity of the D peak $(I_D/I_G = 0.7)$ after cycling corresponds to a small increase in the concentration of defects as the interdefect distance $(L_{\rm D})$ decreases from ~14 to \sim 12 nm.

It should be noted that direct deposition of Zn on the Grmodified Cu substrate is in contrast with the mechanism of Li deposition on the Gr-modified Cu. In fact, it is suggested that Li ions diffuse through the inherent defect sites of the Gr layer and deposit on the Cu substrate where free electrons are available for reduction of Li ions and Gr acts as a mechanical barrier for dendrite growth suppression. 70-73 This behavior can be explained by the lower binding energy of Li (lithiophilicity) to carbon compared to Cu, studied by means of DFT calculations,⁷³ and our electrochemical and microscopy tests. For direct comparison between Zn and Li, we evaluated the nucleation overpotential of Li (Figure S24) and compared the lithiophilicity and zincophilicity of the bare and the Gr-modified Cu electrodes (Figure S25). Our results (discussed in detail in the Supporting Information) suggest that the mechanism of Zn electrodeposition of Gr is in contrast to that of Li, where Gr acts as a mechanical protection layer for suppression of Li dendrites.

Finally, to evaluate the deposition morphology at the current collector/Zn interface, we performed SEM imaging and atomic force microscopy (AFM) analysis on the surface of the delaminated Zn layers. As it can be seen in Figure 5C, the deposition morphology is highly nonhomogeneous even from the initial stages of deposition on the bare Cu, unlike the highly uniform interface observed for the Gr-modified electrode (Figure 5D). Randomly oriented Zn plates formed on the bare Cu have further developed into branched Zn dendrites and led to a very high surface roughness, as characterized by the AFM analysis shown in Figure 5E. A typical structure observed on the Zn/Cu interface is shown to have a 1.6 μ m height difference from the well to the peak. On the other hand, the highly uniform Zn morphology with a smaller surface roughness (\sim 0.7 μ m) shows a typical difference of \sim 0.45 um (Figure 5F) at the interface of Zn/Gr/Cu. This observation confirms the effectiveness of Gr in homogenizing the electrodeposition of Zn. Also, the tilted SEM image in Figure S26 explicates the smooth interface of Gr/Zn versus Cu/Zn. Considering the nucleation analysis at the interface of Zn/Gr/Cu shown in Figure 5, persistence of Gr on the Cu

surface after long cycling (Figures S22 and S23), and the zincophilicity study in Figure S25, we can confidently propose Gr as a zincophilic substrate for uniform deposition of planar

To better understand the mechanism of uniform Zn deposition onto the surface of the Gr-modified electrode, we utilized density functional theory (DFT) to compare the binding energies of Zn to graphene and Cu. It is known that high interaction (binding energy) between the depositing metal and dissimilar substrate is a promoting factor for uniform metal electrodeposition. For this purpose, binding energies of Zn to Cu and Gr were calculated (Figure 6). As shown in Figure 6A,B, the binding energies of Zn to Cu (200) and (111) surfaces (favorable facet terminations)⁷⁴ are -0.21 and -0.86eV, respectively. Considering the highly defective nature of the CVD-grown Gr,³⁷ we considered pristine and defective graphene (one to four defect sites) for calculating the binding energy between Zn and Gr. Zn adsorption onto the nondefective Gr surface (Figure 6C) is -0.02, which is lower compared to that of the bare Cu. However, by creating only one defect site in Gr (Figure 6D), the binding energy of Zn increases significantly (-1.26 eV), making Gr a more attractive deposition substrate for Zn adatoms compared to Cu surface due to the high zincophilicity of Gr. Increasing the number of defect sites to four in the surface of Gr (Figure 6E), the ultrahigh stability of Zn is observed (-4.41 eV in total; 1.1)eV per adatom). We also considered other defective configurations such as double vacancy of Gr (Figure S27); however, only single-vacancy defects are favorable for Zn adsorption.

To determine Zn adsorption preferences between the defective Gr and the Zn surface itself, Zn binding energy to the Zn (0001) surface was calculated. Interestingly, Zn adatoms adsorption on the Zn (0001) surface leads to an increase in energy by ~0.5 eV/adatom (Figure S28), depending on the type of adsorption sites (e.g., on-top, bridge, fcc, and hcp). Therefore, due to the higher bonding energy of Zn atoms to graphene defects compared to other Zn atoms, it can be concluded that Zn adatoms prefer to occupy the defect sites of the Gr substrate at the initial nucleation stage. Additionally, formation of Zn-Zn bonds will not take place until all the defect sites are occupied. This leads to a uniform dispersion of Zn nuclei on the randomly distributed defect sites of the Gr layer. The Zn adatoms have a very small binding energy with the pristine Gr layer (0.02 eV) and only physisorb on the Gr layer, thus have a high mobility over the Gr layer. 75 Therefore, following to full occupation of Gr defect sites and uniform nucleation, the Zn adatoms can freely move and reach to the deposited Zn nuclei and allow for lateral growth of Zn nuclei, leading to the experimentally observed dense and uniform Zn structures (see Figures 2B and 4D). These findings demonstrate that Gr defect sites guide the initial Zn deposition at the nucleation stage, and afterward, subsequent Zn atoms follow the pattern forming epitaxial Zn plates on the Gr surface, as observed in our experimental study (see Figures 2B and 4D).

In addition, the interfacial energy is a critical parameter that indicates the stability and morphology of a deposition metal/ substrate couple. In this context, the crystallographic properties of the electrodepositing metal and the substrate are important parameters that influence the interfacial energy and dictate the nucleation and growth morphology during electrodeposition.³⁰ The interfacial energy increases with the crystal structure mismatch between the two solid phases.⁶⁷ Lattice mismatches is defined as the relative difference between the in-plane lattice constants, which are very close for Zn and Gr, 266 and 246 pm, respectively,²⁹ while the lattice parameter of Cu (361 pm) is much larger. Notably, both Zn and Gr have hexagonal lattice structures, whereas Cu has a face-centered cubic (fcc) structure. Furthermore, we calculated the interfacial energy and the work of separation between Zn and Gr to understand the stability of both interfaces and the energy necessary to create them. Figure \$29 shows the optimized Zn/Gr interface, where four defects are dispersed in the Gr monolayer. The interfacial energy, defined as the difference between the total slab energy and the sum of each slab energy divided by the interface area, is 0.212 J/m². We also studied the interaction of the Zn (0001)/Cu (200) interface. The interfacial energy for the Zn/Cu interface was calculated to be 1.2 J/m², which is significantly higher than that of Zn/Gr (0.212 J/m²), making Gr a better substrate for Zn deposition. From such explanations and calculations of binding energy and the work of separation, the smaller overpotential barrier for Zn deposition on the Gr substrate is explained.

The work of separation, which is the binding energy between the Gr layer and the Zn slab as a function of the interslab distance, was calculated. As can be seen in Figure S30, the equilibrium distance is 3 Å for which the binding energy has the most negative value. As shown in Figure S31, the optimization of initially equally strained surfaces (i.e., 2.3%) leads to a significant change in the Zn (0001) surface indicating a possibility for a nonuniform deposit. Since the adsorption of Zn onto the defective Gr surface is a favorable process, we considered Zn diffusion through the Gr surface (Figure S32). As revealed by our DFT calculations, Zn diffusion through the Gr defective sheet has a very high activation energy of 2.4 eV. Thus, comparing the Zn binding energy onto the Gr surface and its diffusion through the Gr surface, the adsorption is more preferable, which leads to the electrodeposition over the Gr.

CONCLUSIONS

Successful modification of Zn electrodeposition morphology was achieved by utilizing a monolayer graphene film, directly grown on the Cu current collector surface, as the electrodeposition substrate. By employing the Gr-modified substrate, a significant improvement in the battery cycle life up to 400 cycles at a current density of 5 mA/cm² was achieved. This improved performance is attributed to the formation of dense, highly crystalline Zn pallets in the (001) direction parallel to the Gr-modified electrode surface. As a result, the capacity degradation was suppressed significantly in the Gr-modified electrode by limiting the surface protuberances as major nucleation sites of Zn dendrites that coexist on the nonmodified electrode surface. Meanwhile, this approach increases the corrosion resistance of Cu making it a suitable current collector for aqueous Zn batteries. Utilizing a variety of experimental analyses and theoretical calculations, we revealed the mechanism for the altered Zn deposition behavior in the presence of the Gr substrate. The Gr layer acts as a zincophilic substrate, which adsorbs Zn ions to its inherent defect sites. Zn ions spread uniformly all over the Gr surface and nucleate with almost no nucleation overpotential. Upon further deposition, Zn crystals with low lattice mismatch and interfacial energy with the Gr substrate develop into compact Zn pallets conformal with the current collector surface.

METHODS

Graphene-Modified Electrode Fabrication

Copper foil was initially treated for 15 min in hydrochloric acid (10% diluted in deionized water) and rinsed properly with water before cleaning them further with acetone and isopropanol. The cleaned samples were immediately dried with an argon (Ar) gas flow and loaded into the CVD chamber. After properly loading the samples in the center of the CVD tube, the chamber was evacuated (down to 1 mtorr) and then heated up to 1000 °C (with a heating rate of 20 °C/ min) with the protection of 7 sccm hydrogen gas flowing inside to remove possible contaminations. The samples were then annealed under H₂ flow for 30 mins. Annealing in H₂ helps in improving the Cu surface quality by reducing the concentration of nucleation points. The graphene growth was then carried out by introducing 5 sccm of methane (CH₄) for 40 min to obtain the full coverage graphene. The samples were then rapidly cooled down to room temperature and taken out. The obtained Gr-coated Cu sheets were cut into smaller pieces and directly used as Gr-modified electrodes.

Cycling and Electrochemical Measurements

All the electrochemical tests were carried out in a Bio-Logic VMP3 electrochemical workstation equipped with EC-Lab software. Two-electrode 2032 coin-type cells were used for cycling tests. Bare Cu foil electrode and CVD-grown graphene on the Cu foil electrode with an area of ~ 2 cm² were used as working electrodes. Metallic Zn foil was cleaned initially in diluted nitric acid (10%) and water and was employed as a counterelectrode. Glass fiber membrane soaked in the 2 M ZnSO₄ (pH ~4) electrolyte was used as a separator. For Zn plating/stripping tests, a constant current of 5 mA/cm² was applied for 1 h during deposition (discharge) and stripping (charge) voltage was limited to 1 V (vs Zn²⁺/Zn). Nucleation overpotential and potentiodynamic polarization tests were performed using EL-CELL, ECC-AIR 3 electrode cell in which Zn metal was used as both reference and counter electrodes and bare Cu/Gr-modified Cu as the working electrode. The potentiodynamic polarization measurements were performed from -250 to +700 mV versus OCP with a scan rate of 5 mV/ s. Cu and Gr-modified Cu were combined with the Pt counterelectrode in the 2 M ZnSO₄ electrolyte at open circuit voltage for the EIS measurement. R_1 is the electrolyte resistance, surface coating is represented by a constant phase element, Q_1 , and a pore resistance R_2 while the metal/ electrolyte interface is represented by a capacitance, Q₂, and a resistance R_3 . R_2 in the Cu sample represents native copper oxide/hydroxides and in the Gr-modified Cu sample represents graphene coating. The corrosion resistance is the mathematical sum of R_2 and R_3 .

SEM Imaging

Reith e-LiNE 100 electron beam lithography system was used for SEM imaging. SEM experiments were performed with an acceleration voltage of 10 kV and a working distance of 10 mm.

Grazing Incidence X-ray Diffraction (GIXRD)

GIXRD was conducted on a Bruker D8 ADVANCE diffractometer, Cu K α source operated at 40 kV and 40 mA, 2° incidence above selected 2θ with a parallel X-ray beam setup.

X-ray Photoelectron Spectroscopy (XPS)

A Thermo Scientific ESCALAB 250Xi instrument was used to obtain XPS results. The substrates were carefully washed by

acetone, IPA, and deionized water before experiment to remove the solvent residues. All spectra were calibrated based on the C–C bond binding energy at 284.8 eV. Thermo Avantage software was used to analyze and process each element's data. For depth profiling experiments, an Ar ion beam of 4.8 keV energy was used. The instrument is calibrated with an X-ray spot of 500 μ m (sputter area, 2.5 mm in diameter) on silicon, and the etch rate is ~2 nm/10 s. Depth profile analysis was carried out using a 100 s etch step size, which corresponds to ~20 nm of etching in each step.

Raman Spectroscopy

Gr films grown on Cu were transferred on $\mathrm{Si/SiO_2}$ before the measurement due to a much larger Raman scattering intensity and lower spectral background on $\mathrm{Si/SiO_2}$ compared to the Cu substrate. Raman results were obtained from a Renishaw inVia Reflex Raman system equipped with a green 532 nm/50 mW diode-pumped solid-state laser. Spectroscopy was performed using a 50× objective lens. Dwell time and laser strength were set to 10 s and 10% respectively to obtain the best signal-tonoise ratio and avoid the laser-induced damage in the samples.

Atomic Force Microscopy (AFM)

A Bruker-Nano Dimension ICON Dimension was used to obtain the topography map of the Zn surface. NanoScope Analysis software was used for data analysis.

STEM Images and EELS Spectroscopy

All the STEM characterizations were obtained using a JEOL JEM-ARM200CF STEM equipped with a cold field emission gun with a 0.78 Å spatial resolution at 80 kV and a Gatan Enfina EELS system. EELS spectra were collected with a step size of 1 nm.

DFT Calculations

DFT calculations are performed using the Vienna ab initio simulations package (VASP) code employing the generalized gradient approximation (GGA) using the PBE (Perdew, Burke, and Ernzerhof) functional to account for the exchangecorrelation effects. In addition, to account for the Coulombic repulsion between localized electrons in Cu and Zn, the DFT + U schema is used. The Hubbard parameters (U-I) for Cu and Zn are set as 5 and 7.5, respectively. For systems with an even number of electrons, nonspin-polarized calculations are performed, and for systems with an odd number of electrons, unrestricted spin-polarized calculations are performed. For all calculations, a cutoff energy of 500 eV is used. All structural optimizations are carried out until the forces, acting on atoms, are below 0.01 eV/Å. The criterion for energy change is set to 0.1 eV. The Atomistic Tool Kit (ATK) is used to build the Zn/ Gr interface, where the "Interface Builder" tool allows analyzing all possible interfaces between the Zn slab and Gr monolayer. The ATK "Interface Builder" algorithm searches all possible structures of the two surfaces to find a configuration with minimal strain. Since there are tens of possibilities between Zn and Gr surfaces, we apply specific cutoff conditions, such as the strain of each surface should not be more than 5% and a total number of atoms in the resulting structure should not exceed 350 atoms (due to natural DFT limitation). The resulting structures were optimized with different widths between the surfaces to find the most stable configuration. The final most favorable structure is shown in Figure S19.

ASSOCIATED CONTENT

S Supporting Information

The Supporting Information is available free of charge at https://pubs.acs.org/doi/10.1021/acsami.9b13174.

OM, SEM, XPS, and Raman spectra of CVD-grown Gr before and after cycling; OM, EIS, and Tafel plot of corrosion test; SEM images, EDS, and GIXRD of electrodeposited Zn. Comparison between Zn and Li electrodeposition on Gr by overpotential test and OM; and DFT calculations on stability of Zn on Gr and Cu (PDF)

AUTHOR INFORMATION

Corresponding Author

*E-mail: rsyassar@uic.edu.

ORCID ®

Tara Foroozan: 0000-0003-1334-3048 Vitaliy Yurkiv: 0000-0002-3407-891X Soroosh Sharifi-Asl: 0000-0003-0441-9231 Farzad Mashayek: 0000-0003-1187-4937 Reza Shahbazian-Yassar: 0000-0002-7744-4780

Author Contributions

R.S.-Y. and T.F. conceived the idea and designed the experimental protocols. T.F. performed the CVD graphene synthesis, battery fabrication, electrochemical tests, SEM, AFM, OM, XRD, XPS, and Raman spectroscopy. F.M. led the DFT calculations and modeling. V.Y. conducted the DFT calculations. S.S.-A. carried out TEM characterization and EELS data analysis. R.R. assisted in electrochemical tests. All the authors contributed to the writing and discussion of the manuscript.

Notes

The authors declare no competing financial interest.

■ ACKNOWLEDGMENTS

R.S.-Y. acknowledges the financial support from the National Science Foundation (award no. CMMI 1619743). The authors acknowledge the financial support from the National Science Foundation award no. CBET-1805938. The authors also thank UIC Nanotechnology Core Facility (NCF) for assisting the usage of their equipment and instrumentation. The present DFT calculations were supported by the National Science Foundation Extreme Science and Engineering Discovery Environment (XSEDE) award no. TG-DMR180106 as well as the computing resources provided on Bebop, a high-performance computing cluster operated by the Laboratory Computing Resource Center at Argonne National Laboratory. This work also made use of instruments in the Electron Microscopy Service (Research Resources Center, UIC).

REFERENCES

- (1) Mainar, A. R.; Iruin, E.; Colmenares, L. C.; Kvasha, A.; de Meatza, I.; Bengoechea, M.; Leonet, O.; Boyano, I.; Zhang, Z.; Blazquez, J. A. An Overview of Progress in Electrolytes for Secondary Zinc-Air Batteries and Other Storage Systems Based on Zinc. *J. Energy Storage* 2018, 15, 304–328.
- (2) Konarov, A.; Voronina, N.; Jo, J. H.; Bakenov, Z.; Sun, Y.-K.; Myung, S.-T. Present and Future Perspective on Electrode Materials for Rechargeable Zinc-Ion Batteries. *ACS Energy Lett.* **2018**, *3*, 2620. (3) Turney, D. E.; Gallaway, J. W.; Yadav, G. G.; Ramirez, R.; Nyce,

M.; Banerjee, S.; Chen-Wiegart, Y.-C. K.; Wang, J.; D'Ambrose, M. J.;

- Kolhekar, S. Rechargeable Zinc Alkaline Anodes for Long-Cycle Energy Storage. *Chem. Mater.* **2017**, 29, 4819–4832.
- (4) Ma, L.; Chen, S.; Li, H.; Ruan, Z.; Tang, Z.; Liu, Z.; Wang, Z.; Huang, Y.; Pei, Z.; Zapien, J. A.; et al. Initiating a Mild Aqueous Electrolyte Co₃O₄/Zn Battery with 2.2 V-High Voltage and 5000-Cycle Lifespan by a Co(III) Rich-Electrode. *Energy Environ. Sci.* **2018**, 11, 2521–2530.
- (5) Kang, Z.; Wu, C.; Dong, L.; Liu, W.; Mou, J.; Zhang, J.; Chang, Z.; Jiang, B.; Wang, G.; Kang, F.; et al. 3D Porous Copper Skeleton Supported Zinc Anode toward High Capacity and Long Cycle Life Zinc Ion Batteries. ACS Sustainable Chem. Eng. 2019, 7, 3364–3371.
- (6) Yadav, G. G.; Turney, D.; Huang, J.; Wei, X.; Banerjee, S. Breaking the 2 V Barrier in Aqueous Zinc Chemistry: Creating 2.45 and 2.8 V MnO₂–Zn Aqueous Batteries. *ACS Energy Lett.* **2019**, *4*, 2.144–2.146
- (7) Zhang, L.; Chen, L.; Zhou, X.; Liu, Z. Towards High-Voltage Aqueous Metal-Ion Batteries Beyond 1.5 V: The Zinc / Zinc Hexacyanoferrate System. *Adv. Energy Mater.* **2015**, *5*, 1400930.
- (8) Higashi, S.; Lee, S. W.; Lee, J. S.; Takechi, K.; Cui, Y. Avoiding Short Circuits from Zinc Metal Dendrites in Anode by Backside-Plating Configuration. *Nat. Commun.* **2016**, *7*, 11801.
- (9) Yi, J.; Liang, P.; Liu, X.; Wu, K.; Liu, Y.; Wang, Y.; Xia, Y.; Zhang, J. Challenges, Mitigation Strategies and Perspectives in Development of Zinc-Electrode Materials and Fabrication for Rechargeable Zinc-Air Batteries. *Energy Environ. Sci.* **2018**, *11*, 3075–3095.
- (10) Banik, S. J.; Akolkar, R. Suppressing Dendrite Growth during Zinc Electrodeposition by PEG-200 Additive. *J. Electrochem. Soc.* **2013**, *160*, D519–D523.
- (11) Otani, T.; Fukunaka, Y.; Homma, T. Effect of Lead and Tin Additives on Surface Morphology Evolution of Electrodeposited Zinc. *Electrochim. Acta* **2017**, 242, 364–372.
- (12) Parker, J. F.; Chervin, C. N.; Nelson, E. S.; Rolison, D. R.; Long, J. W. Wiring Zinc in Three Dimensions Re-Writes Battery Performance Dendrite-Free Cycling. *Energy Environ. Sci.* **2014**, *7*, 1117–1124.
- (13) Stock, D.; Dongmo, S.; Miyazaki, K.; Abe, T.; Janek, J.; Schröder, D. Towards Zinc-Oxygen Batteries with Enhanced Cycling Stability: The Benefit of Anion-Exchange Ionomer for Zinc Sponge Anodes. *J. Power Sources* **2018**, 395, 195–204.
- (14) Yan, Z.; Wang, E.; Jiang, L.; Sun, G. Superior Cycling Stability and High Rate Capability of Three-Dimensional Zn/Cu Foam Electrodes for Zinc-Based Alkaline Batteries. *RSC Adv.* **2015**, *5*, 83781–83787.
- (15) Wang, L.-P.; Li, N.-W.; Wang, T.-S.; Yin, Y.-X.; Guo, Y.-G.; Wang, C.-R. Conductive Graphite Fiber as a Stable Host for Zinc Metal Anodes. *Electrochim. Acta* **2017**, *244*, 172–177.
- (16) Lee, B.-S.; Cui, S.; Xing, X.; Liu, H.; Yue, X.; Petrova, V.; Lim, H.-D.; Chen, R.; Liu, P. Dendrite Suppression Membranes for Rechargeable Zinc Batteries. ACS Appl. Mater. Interfaces 2018, 10, 38928–38935.
- (17) Banik, S. J.; Akolkar, R. Suppressing Dendritic Growth during Alkaline Zinc Electrodeposition Using Polyethylenimine Additive. *Electrochim. Acta* **2015**, *179*, 475–481.
- (18) Schmid, M.; Willert-Porada, M. Zinc Particles Coated with Bismuth Oxide Based Glasses as Anode Material for Zinc Air Batteries with Improved Electrical Rechargeability. *Electrochim. Acta* **2018**, 260, 246–253.
- (19) Michlik, T.; Schmid, M.; Rosin, A.; Gerdes, T.; Moos, R. Mechanical Coating of Zinc Particles with Bi₂O₃-Li₂O-ZnO Glasses as Anode Material for Rechargeable Zinc-Based Batteries. *Batteries* **2018**, *4*, 12.
- (20) Shen, C.; Li, X.; Li, N.; Xie, K.; Wang, J.-G.; Liu, X.; Wei, B. Graphene-Boosted, High-Performance Aqueous Zn-Ion Battery. ACS Appl. Mater. Interfaces 2018, 10, 25446—25453.
- (21) Xia, A.; Pu, X.; Tao, Y.; Liu, H.; Wang, Y. Graphene Oxide Spontaneous Reduction and Self-Assembly on the Zinc Metal Surface Enabling a Dendrite-Free Anode for Long-Life Zinc Rechargeable Aqueous Batteries. *Appl. Surf. Sci.* **2019**, *481*, 852–859.

- (22) Zhao, K.; Wang, C.; Yu, Y.; Yan, M.; Wei, Q.; He, P.; Dong, Y.; Zhang, Z.; Wang, X.; Mai, L. Ultrathin Surface Coating Enables Stabilized Zinc Metal Anode. *Adv. Mater. Interfaces* **2018**, 5, 1800848.
- (23) Khor, A.; Leung, P.; Mohamed, M. R.; Flox, C.; Xu, Q.; An, L.; Wills, R. G. A.; Morante, J. R.; Shah, A. A. Review of Zinc-Based Hybrid Flow Batteries: From Fundamentals to Applications. *Mater. Today Energy* **2018**, *8*, 80–108.
- (24) Verma, V.; Kumar, S.; Manalastas, W., Jr.; Satish, R.; Srinivasan, M. Progress in Rechargeable Aqueous Zinc- and Aluminum-Ion Battery Electrodes: Challenges and Outlook. *Adv. Sustainable Syst.* **2019**, *3*, 1800111.
- (25) Wei, X.; Desai, D.; Yadav, G. G.; Turney, D. E.; Couzis, A.; Banerjee, S. Impact of Anode Substrates on Electrodeposited Zinc over Cycling in Zinc-Anode Rechargeable Alkaline Batteries. *Electrochim. Acta* **2016**, *212*, 603–613.
- (26) Ghodsi, S. M.; Megaridis, C. M.; Shahbazian-yassar, R.; Shokuhfar, T. Advances in Graphene-Based Liquid Cell Electron Microscopy: Working Principles, Opportunities, and Challenges. *Small Methods* **2019**, *3*, 1900026.
- (27) Hu, J.; Ji, Y.; Shi, Y.; Hui, F.; Duan, H.; Lanza, M. A Review on the Use of Graphene as a Protective Coating against Corrosion. *Ann. Mater. Sci. Eng.* **2014**, *1*, 1–16.
- (28) Prasai, D.; Tuberquia, J. C.; Harl, R. R.; Jennings, G. K.; Bolotin, K. I. Graphene: Corrosion-Inhibiting Coating. *ACS Nano* **2012**, *6*, 1102–1108.
- (29) Pearson, W. B. A Handbook of Lattice Spacings and Structures of Metals and Alloys; International series of monographs on metal physics and physical metallurgy; Pergamon Press, 1958.
- (30) Gu, Y.; Xu, H.-Y.; Zhang, X.-G.; Wang, W.-W.; He, J.-W.; Tang, S.; Yan, J.-W.; Wu, D.-Y.; Zheng, M.-S.; Dong, Q.-F.; et al. Lithiophilic Faceted Cu(100) Surfaces: High Utilization of Host Surface and Cavities for Lithium Metal Anodes. *Angew. Chem., Int. Ed.* **2019**, 3092–3096.
- (31) Meng, Q.; Deng, B.; Zhang, H.; Wang, B.; Zhang, W.; Wen, Y.; Ming, H.; Zhu, X.; Guan, Y.; Xiang, Y.; et al. Heterogeneous Nucleation and Growth of Electrodeposited Lithium Metal on the Basal Plane of Single-Layer Graphene. *Energy Storage Mater.* **2019**, *16*, 419–425.
- (32) Levchenko, I.; Ostrikov, K. K.; Zheng, J.; Li, X.; Keidar, M.; Teo, K. B. K. Scalable Graphene Production: Perspectives and Challenges of Plasma Applications. *Nanoscale* **2016**, *8*, 10511–10527.
- (33) Xu, Y.; Cao, H.; Xue, Y.; Li, B.; Cai, W. Liquid-Phase Exfoliation of Graphene: An Overview on Exfoliation Media, Techniques, and Challenges. *Nanomaterials* **2018**, *8*, 942.
- (34) Wu, J.-B.; Lin, M.-L.; Cong, X.; Liu, H.-N.; Tan, P.-H. Raman Spectroscopy of Graphene-Based Materials and Its Applications in Related Devices. *Chem. Soc. Rev.* **2018**, *47*, 1822–1873.
- (35) Malard, L. M.; Pimenta, M. A.; Dresselhaus, G.; Dresselhaus, M. S. Raman Spectroscopy in Graphene. *Phys. Rep.* **2009**, *473*, 51–87.
- (36) Sittig, M. Copper and Compounds . Handbook of toxic Hazardous Chemicals and Carcinogens: Noyes Publications, 1985, 2, 256–259.
- (37) Xie, J.; Liao, L.; Gong, Y.; Li, Y.; Shi, F.; Pei, A.; Sun, J.; Zhang, R.; Kong, B.; Subbaraman, R.; et al. Stitching H-BN by Atomic Layer Deposition of LiF as a Stable Interface for Lithium Metal Anode. *Sci. Adv* **2017**, *3*, eaao3170.
- (38) Wang, Z.; Huang, J.; Guo, Z.; Dong, X.; Liu, Y.; Wang, Y.; Xia, Y. A Metal-Organic Framework Host for Highly Reversible Dendrite-Free Zinc Metal Anodes. *Joule* **2019**, *3*, 1289–1300.
- (39) Singh Raman, R. K.; Chakraborty Banerjee, P.; Lobo, D. E.; Gullapalli, H.; Sumandasa, M.; Kumar, A.; Choudhary, L.; Tkacz, R.; Ajayan, P. M.; Majumder, M. Protecting Copper from Electrochemical Degradation by Graphene Coating. *Carbon* **2012**, *50*, 4040–4045.
- (40) Bu, I. Y. Y.; Fu, Y.-S.; Li, J.-F.; Guo, T.-F. Large-Area Electrospray-Deposited Nanocrystalline CuXO Hole Transport Layer for Perovskite Solar Cells. *RSC Adv.* **2017**, *7*, 46651–46656.

- (41) Nam, T.-H.; Lee, J.-H.; Choi, S.-R.; Yoo, J.-B.; Kim, J.-G. Graphene Coating as a Protective Barrier against Hydrogen Embrittlement. *Int. J. Hydrogen Energy* **2014**, *39*, 11810–11817.
- (42) Kirkland, N. T.; Schiller, T.; Medhekar, N.; Birbilis, N. Exploring Graphene as a Corrosion Protection Barrier. *Corros. Sci.* **2012**, *56*, 1–4.
- (43) Azhagurajan, M.; Nakata, A.; Arai, H.; Ogumi, Z.; Kajita, T.; Itoh, T.; Itaya, K. Effect of Vanillin to Prevent the Dendrite Growth of Zn in Zinc-Based Secondary Batteries. *J. Electrochem. Soc.* **2017**, *164*, A2407—A2417.
- (44) Otani, T.; Nagata, M.; Fukunaka, Y.; Homma, T. Morphological Evolution of Mossy Structures during the Electrodeposition of Zinc from an Alkaline Zincate Solution. *Electrochim. Acta* **2016**, 206, 366–373.
- (45) Wang, R. Y.; Kirk, D. W.; Zhang, G. X. Effects of Deposition Conditions on the Morphology of Zinc Deposits from Alkaline Zincate Solutions. *J. Electrochem. Soc.* **2006**, *153*, C357.
- (46) Sawada, Y. Transition of Growth Form from Dendrite to Aggregate. *Phys. A* **1986**, *140*, 134–141.
- (47) Sun, K. E. K.; Hoang, T. K. A.; Doan, T. N. L.; Yu, Y.; Chen, P. Highly Sustainable Zinc Anodes for a Rechargeable Hybrid Aqueous Battery. *Chem. Eur. J.* **2018**, *24*, 1667–1673.
- (48) Mackinnon, D. J.; Brannen, J. M.; Fenn, P. L. Characterization of Impurity Effects in Zinc Electrowinning from Industrial Acid Sulphate Electrolyte. *J. Appl. Electrochem.* **1987**, *17*, 1129–1143.
- (49) Cachet, C.; Saïdani, B.; Wiart, R. The Kinetics of Zinc Deposition at Low Overpotentials in Alkaline Electrolytes. *Electrochim. Acta* 1988, 33, 405–416.
- (50) Dong, L.; Ma, X.; Li, Y.; Zhao, L.; Liu, W.; Cheng, J.; Xu, C.; Li, B.; Yang, Q.-H.; Kang, F. Extremely Safe, High-Rate and Ultralong-Life Zinc-Ion Hybrid Supercapacitors. *Energy Storage Mater.* **2018**, *13*, 96–102.
- (51) Li, Y.; Li, Y.; Pei, A.; Yan, K.; Sun, Y.; Wu, C.-L.; Joubert, L. M.; Chin, R.; Koh, A. L.; Yu, Y.; et al. Atomic Structure of Sensitive Battery Materials and Interfaces Revealed by Cryo-electron Microscopy. *Science* **2017**, 358, 506–510.
- (52) Alias, N.; Mohamad, A. A. Morphology Study of Electrodeposited Zinc from Zinc Sulfate Solutions as Anode for Zinc-Air and Zinc-Carbon Batteries. J. King Saud Univ., Eng. Sci. 2015, 27, 43–48.
- (53) Steiger, J.; Kramer, D.; Mönig, R. Mechanisms of Dendritic Growth Investigated by in Situ Light Microscopy during Electrodeposition and Dissolution of Lithium. *J. Power Sources* **2014**, 261, 112–119.
- (54) Gu, W.; Liu, C.; Tang, J.; Liu, R.; Yang, H.; Hu, J. Improving Zinc Electrodeposition in Ammoniacal Electrolytes with the Saturated Dissolved Methyltrioctylammonium Chloride. *Hydrometallurgy* **2018**, 175, 43–51.
- (55) Raeissi, K.; Saatchi, A.; Golozar, M. A. Effect of Nucleation Mode on the Morphology and Texture of Electrodeposited Zinc. *J. Appl. Electrochem.* **2003**, *33*, 635–642.
- (56) Horn, Q. C.; Shao-Horn, Y. Morphology and Spatial Distribution of ZnO Formed in Discharged Alkaline Zn/MnO[Sub 2] AA Cells. J. Electrochem. Soc. 2003, 150, A652.
- (57) Wu, T.-H.; Zhang, Y.; Althouse, Z. D.; Liu, N. Nanoscale Design of Zinc Anodes for High-Energy Aqueous Rechargeable Batteries. *Mater. Today Nano* **2019**, *6*, 100032.
- (58) Vijayaratnam, V.; Natter, H.; Grandthyll, S.; Neurohr, J. U.; Jacobs, K.; Müller, F.; Hempelmann, R. Unwanted Electroless Zinc Plating on Current Collectors in Zinc Air Batteries. 2017, arXiv:1706.05929. arXiv.org e-Print archive. Condens. Matter, 1–10. https://arxiv.org/abs/1706.05929.
- (59) Beverskog, B.; Puigdomenech, I. Revised Pourbaix Diagrams for Zinc at 25–300 °C. Corros. Sci. 1997, 107.
- (60) Lai, S.-B.; Jamesh, M.-I.; Wu, X.-C.; Dong, Y.-L.; Wang, J.-H.; Gao, M.; Liu, J.-F.; Sun, X.-M. A Promising Energy Storage System: Rechargeable Ni–Zn Battery. *Rare Met.* **2017**, *36*, 381–396.
- (61) Lee, B.; Seo, H. R.; Lee, H. R.; Yoon, C. S.; Kim, J. H.; Chung, K. Y.; Cho, B. W.; Oh, S. H. Critical Role of PH Evolution of

- Electrolyte in the Reaction Mechanism for Rechargeable Zinc Batteries. ChemSusChem 2016, 9, 2948–2956.
- (62) Pei, A.; Zheng, G.; Shi, F.; Li, Y.; Cui, Y. Nanoscale Nucleation and Growth of Electrodeposited Lithium Metal. *Nano Lett.* **2017**, *17*, 1132–1139.
- (63) Zhang, R.; Chen, X.-R.; Chen, X.; Cheng, X.-B.; Zhang, X.-Q.; Yan, C.; Zhang, Q. Lithiophilic Sites in Doped Graphene Guide Uniform Lithium Nucleation for Dendrite-Free Lithium Metal Anodes. *Angew. Chem., Int. Ed.* **2017**, *56*, 7764–7768.
- (64) Yang, C.; Yao, Y.; He, S.; Xie, H.; Hitz, E.; Hu, L. Ultrafine Silver Nanoparticles for Seeded Lithium Deposition toward Stable Lithium Metal Anode. *Adv. Mater.* **2017**, *29*, 1702714.
- (65) Jin, C.; Sheng, O.; Luo, J.; Yuan, H.; Fang, C.; Zhang, W.; Huang, H.; Gan, Y.; Xia, Y.; Liang, C.; et al. 3D Lithium Metal Embedded within Lithiophilic Porous Matrix for Stable Lithium Metal Batteries. *Nano Energy* **2017**, *37*, 177–186.
- (66) Chi, S.-S.; Liu, Y.; Song, W.-L.; Fan, L.-Z.; Zhang, Q. Prestoring Lithium into Stable 3D Nickel Foam Host as Dendrite-Free Lithium Metal Anode. *Adv. Funct. Mater.* **2017**, *27*, 1700348.
- (67) Yan, K.; Lu, Z.; Lee, H.-W.; Xiong, F.; Hsu, P.-C.; Li, Y.; Zhao, J.; Chu, S.; Cui, Y. Selective Deposition and Stable Encapsulation of Lithium through Heterogeneous Seeded Growth. *Nat. Energy* **2016**, *1*, 16010.
- (68) Li, G.-R.; Dawa, C.-R.; Bu, Q.; Lu, X.-H.; Ke, Z.-H.; Hong, H.-E.; Zheng, F.-L.; Yao, C.-Z.; Liu, G.-K.; Tong, Y.-X. Electrochemical Self-Assembly of ZnO Nanoporous Structures. *J. Phys. Chem. C* **2007**, *111*, 1919–1923.
- (69) Lucchese, M. M.; Stavale, F.; Ferreira, E. H. M.; Vilani, C.; Moutinho, M. V. O.; Capaz, R. B.; Achete, C. A.; Jorio, A. Quantifying Ion-Induced Defects and Raman Relaxation Length in Graphene. *Carbon* **2010**, *48*, 1592–1597.
- (70) Zhang, R.; Wen, S.; Wang, N.; Qin, K.; Liu, E.; Shi, C.; Zhao, N. N-Doped Graphene Modified 3D Porous Cu Current Collector toward Microscale Homogeneous Li Deposition for Li Metal Anodes. *Adv. Energy Mater.* **2018**, *8*, 1800914.
- (71) Yan, K.; Lee, H.-W.; Gao, T.; Zheng, G.; Yao, H.; Wang, H.; Lu, Z.; Zhou, Y.; Liang, Z.; Liu, Z.; Chu, S.; Cui, Y. Ultrathin Two-Dimensional Atomic Crystals as Stable Interfacial Layer for Improvement of Lithium Metal Anode. *Nano Lett.* **2014**, *14*, 6016–6022.
- (72) Zhang, C.; Wang, A.; Zhang, J.; Guan, X.; Tang, W.; Luo, J. 2D Materials for Lithium/Sodium Metal Anodes. *Adv. Energy Mater.* **2018**, *8*, 1802833.
- (73) Foroozan, T.; Soto, F. A.; Yurkiv, V.; Sharifi-Asl, S.; Deivanayagam, R.; Huang, Z.; Rojaee, R.; Mashayek, F.; Balbuena, P. B.; Shahbazian-Yassar, R. Synergistic Effect of Graphene Oxide for Impeding the Dendritic Plating of Li. *Adv. Funct. Mater.* **2018**, 28, 1705917.
- (74) Patra, A.; Bates, J. E.; Sun, J.; Perdew, J. P. Properties of Real Metallic Surfaces: Effects of Density Functional Semilocality and van Der Waals Nonlocality. *Proc. Natl. Acad. Sci. U. S. A.* **2017**, *114*, E9188–E9196.
- (75) Lu, Y.; Tu, Z.; Archer, L. A. Stable Lithium Electrodeposition in Liquid and Nanoporous Solid Electrolytes. *Nat. Mater.* **2014**, *13*, 961–969.